Supplementary information

Improved reverse water-gas shift chemical looping performance of Co–In-based oxygen carriers supported on ceria

Takuma Higo*, Shuhei Ishizaki, Kenji Ichizuka, Yasushi Sekine*

This file includes:

Figures. S1 to S17

Tables S1 to S10

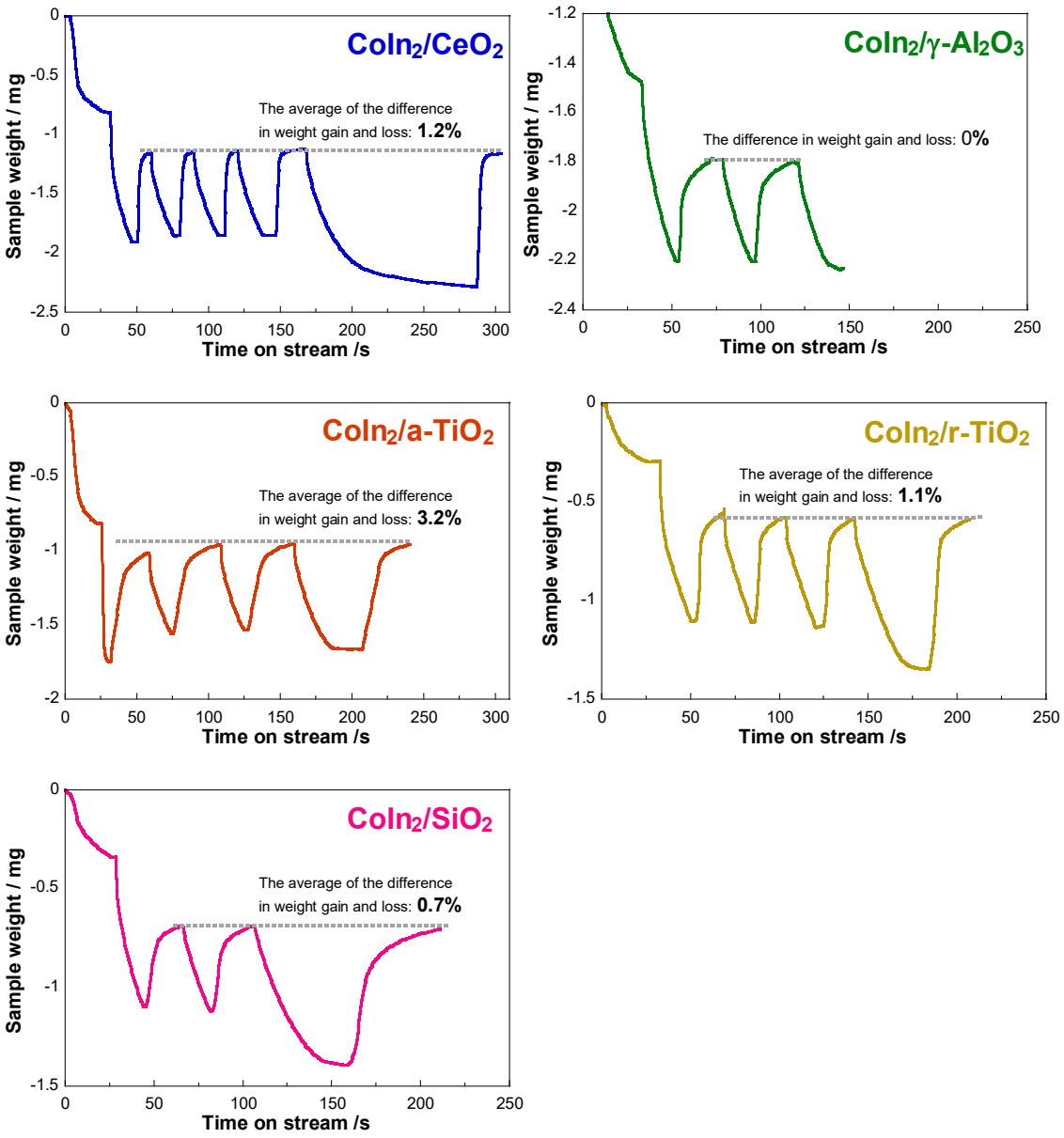

Figure S1. The TGA curves of OCs during RWGS-CL cycle.

In the TGA profiles, weight loss corresponds to oxygen release during the reduction step, while weight gain corresponds to oxygen uptake during the oxidation step. The first cycle shows a larger weight change due to the additional reduction of oxidized Co species. Therefore, the subsequent cycles (from the second cycle onward), which primarily reflect the redox behavior of In species, were used for evaluation.

The difference between weight loss and weight gain in these cycles was found to be within 0–3.2%, corresponding to 0–0.19 mmol g^{-1} in terms of oxygen amount. These results indicate that the lattice oxygen released from the oxygen carriers, including both In species and the support, is almost fully regenerated during the redox cycles.

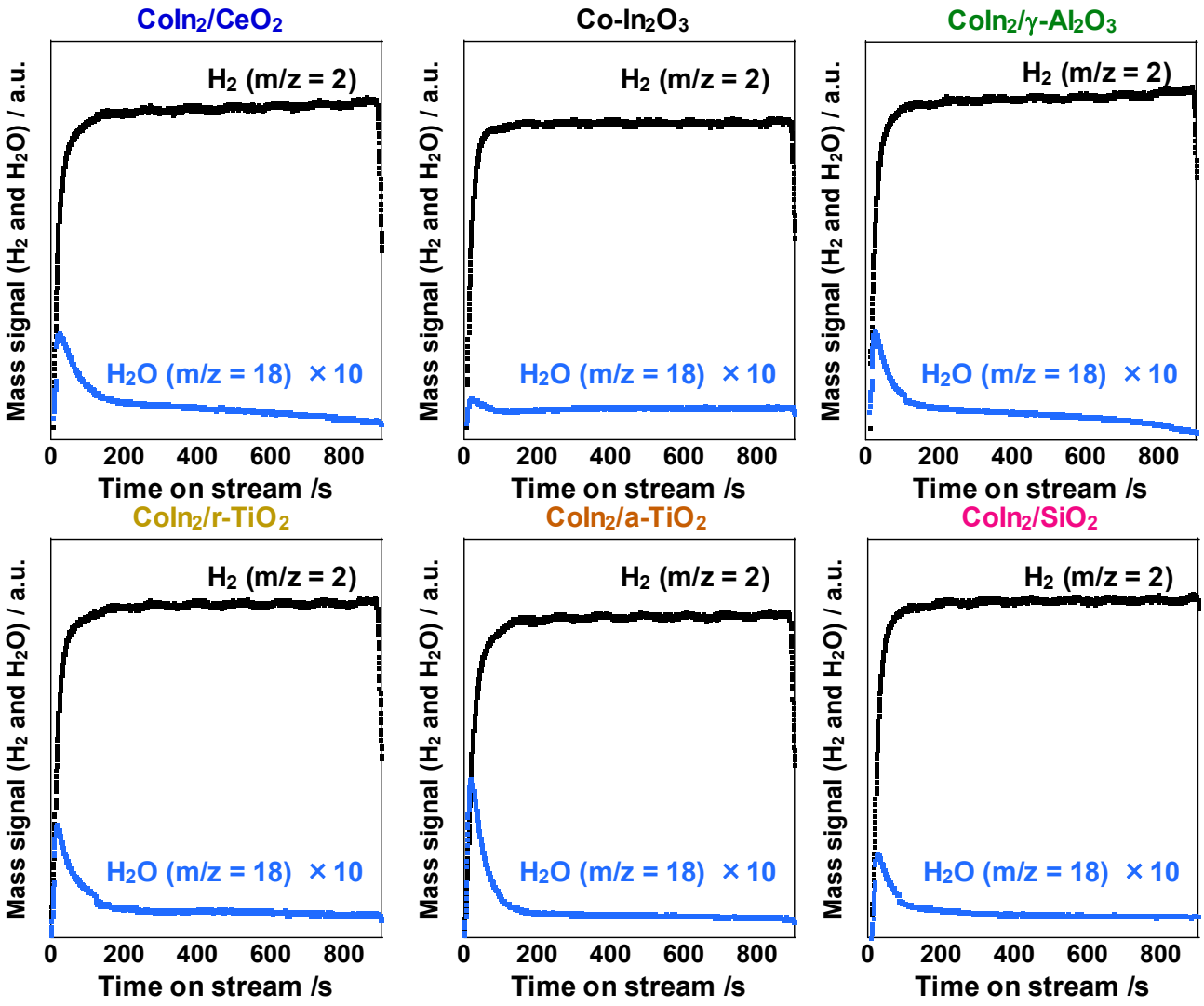

Figure S2. Mass signal of H_2 (m/z = 2) and H_2O (m/z = 18) on the prepared OCs (20wt% $CoIn_2/CeO_2$, Co-In_2O_3, 20wt% $CoIn_2/\gamma$-Al_2O_3, 20wt% $CoIn_2$/r-TiO_2, 20wt% $CoIn_2$/a-TiO_2 and 20wt% $CoIn_2/SiO_2$) during the reduction step.

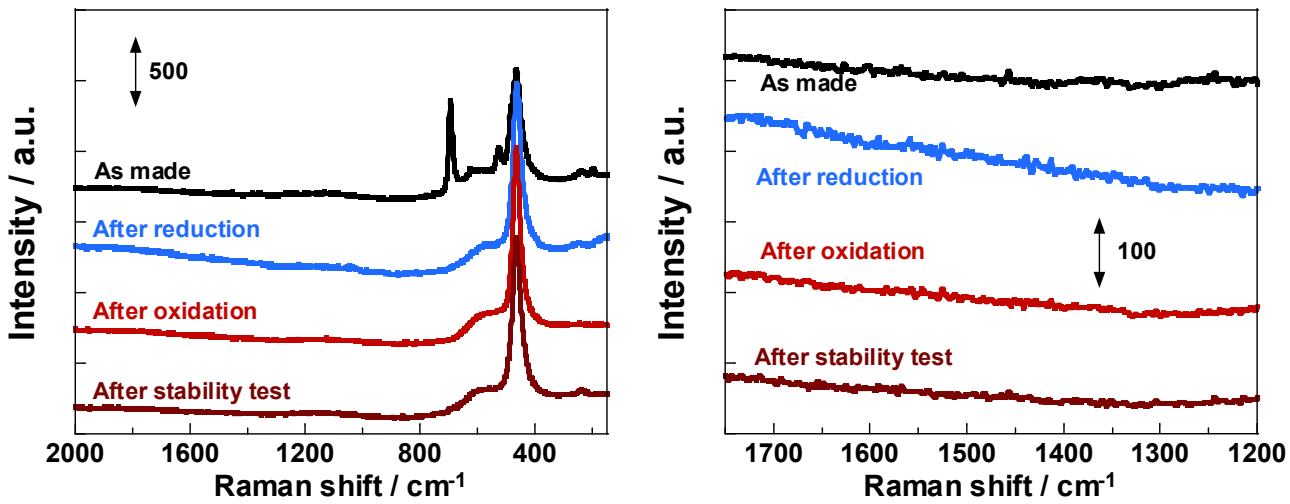

Figure S3. Raman spectra of 20wt% $CoIn_2/CeO_2$ (As-prepared, after reduction step, after oxidation step and after the stability test).

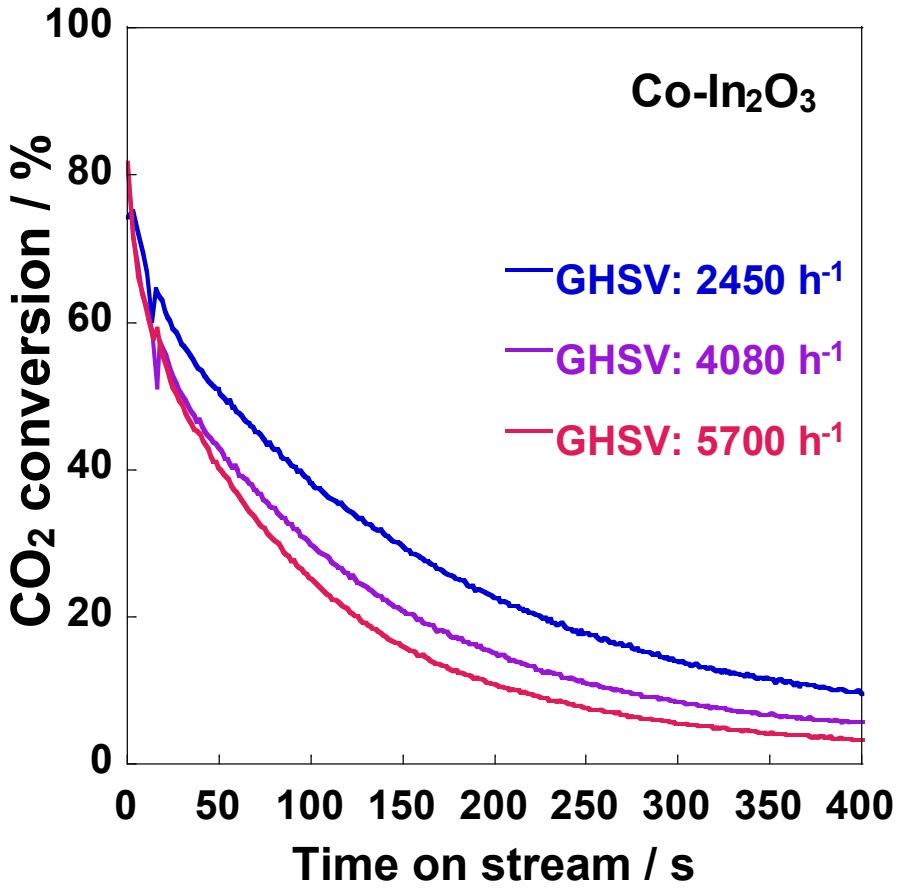

Figure S4 CO_2 conversion on 20wt% $CoIn_2/CeO_2$ during the oxidation step using 100vol% CO_2.

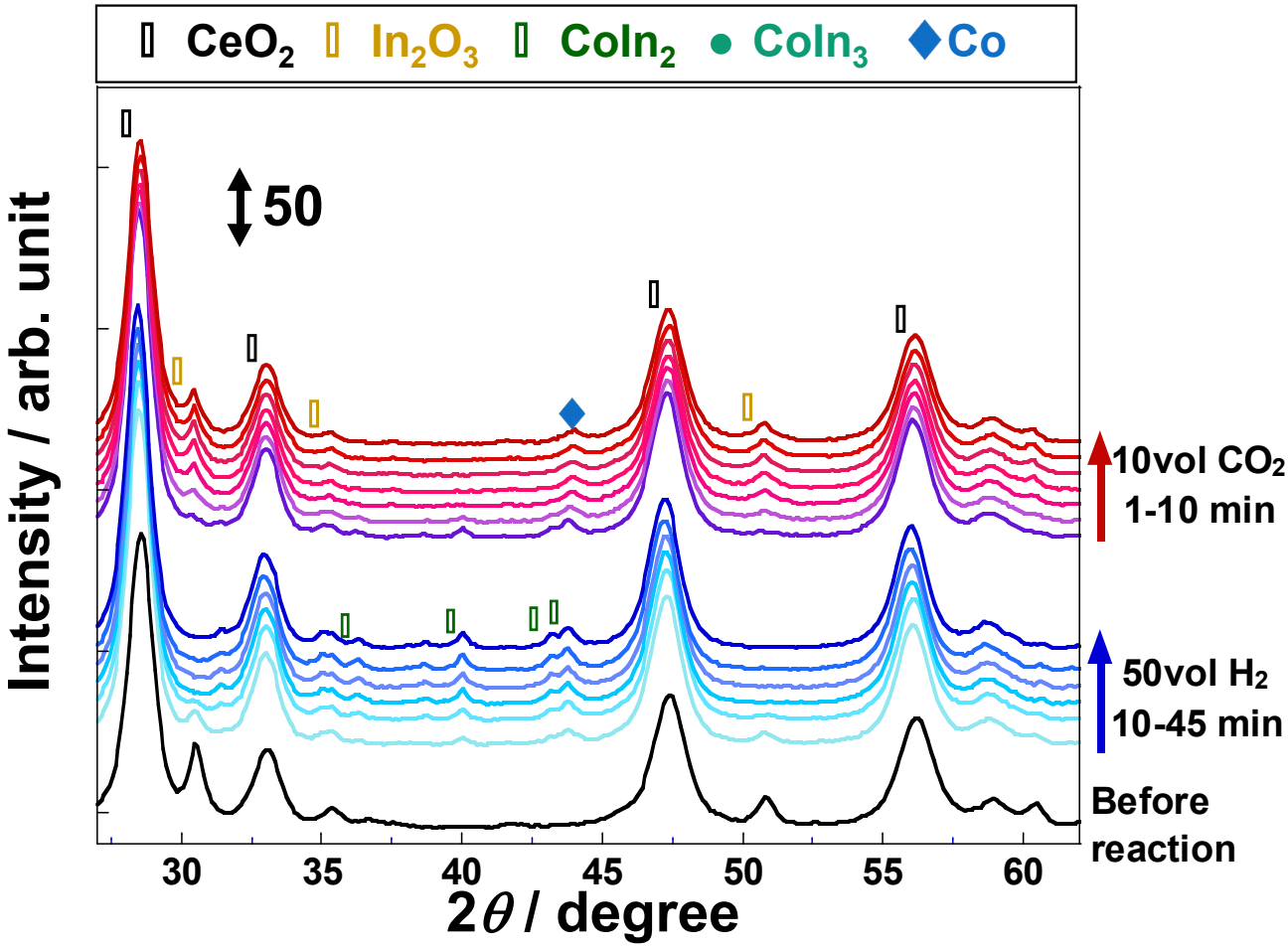

Figure S5 *In-situ* XRD results of 20wt% $CoIn_2/CeO_2$ under 50vo% H_2 (reduction step) and 10vol% CO_2 (oxidation step) at 773 K.

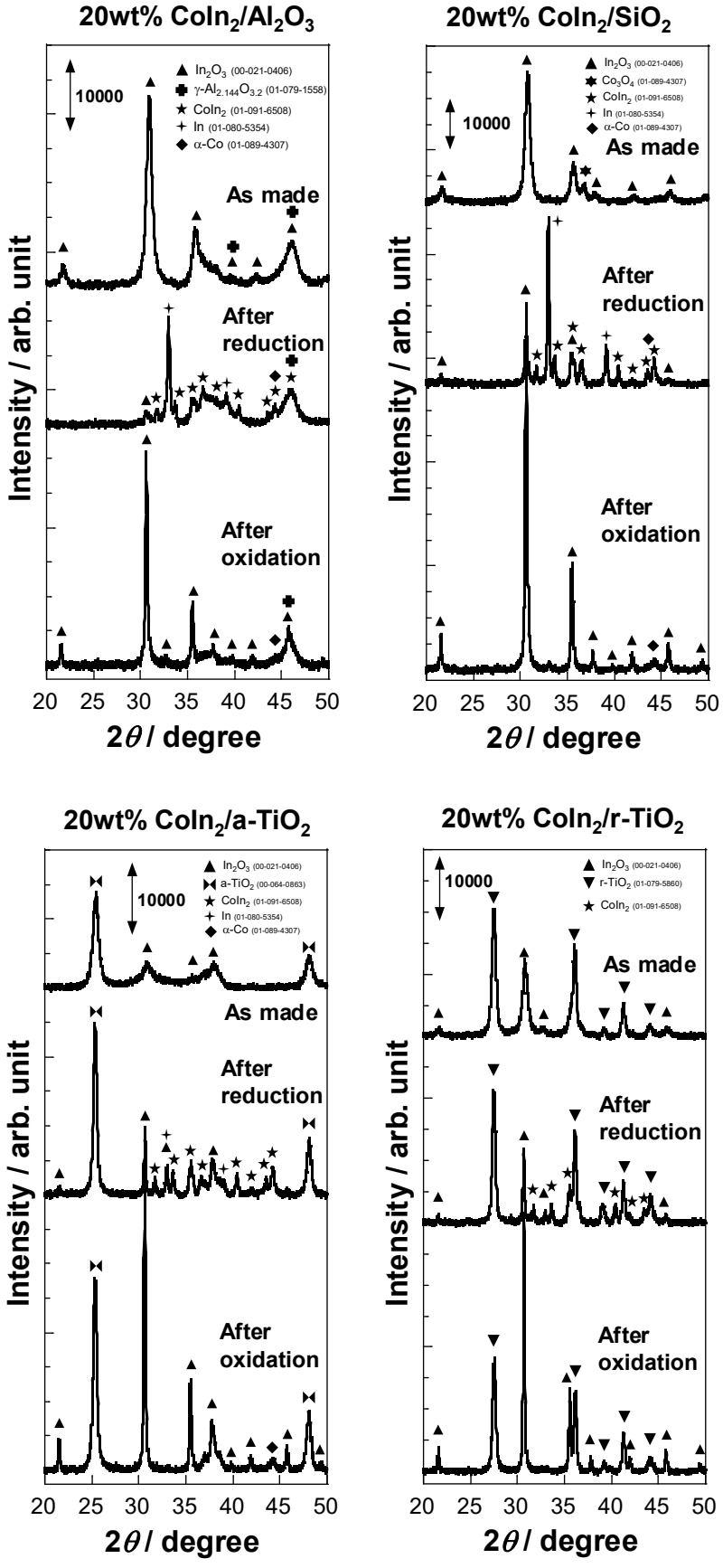

Figure S6 XRD patterns of $CoIn_2$ supported OCs before and after RWGS-CL cycle.

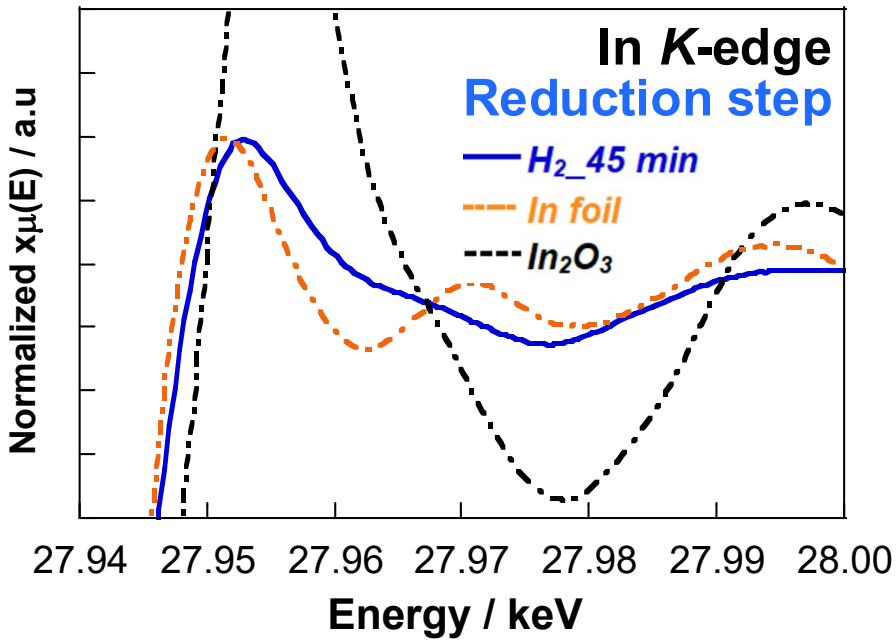

Figure S7 Enlarged view near the isosbestic point in the *in-situ* XANES spectra during reduction.

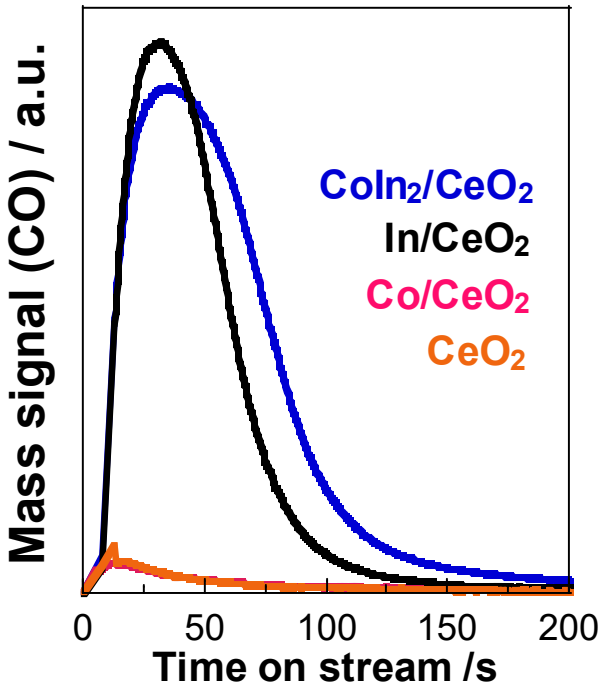

Figure S8 Mass signal of CO (m/z = 28) on the prepared OCs (20wt% $CoIn_2/CeO_2$, 15.9wt% In/CeO_2, 4.1wt% Co/CeO_2 and CeO_2) at the oxidation step.

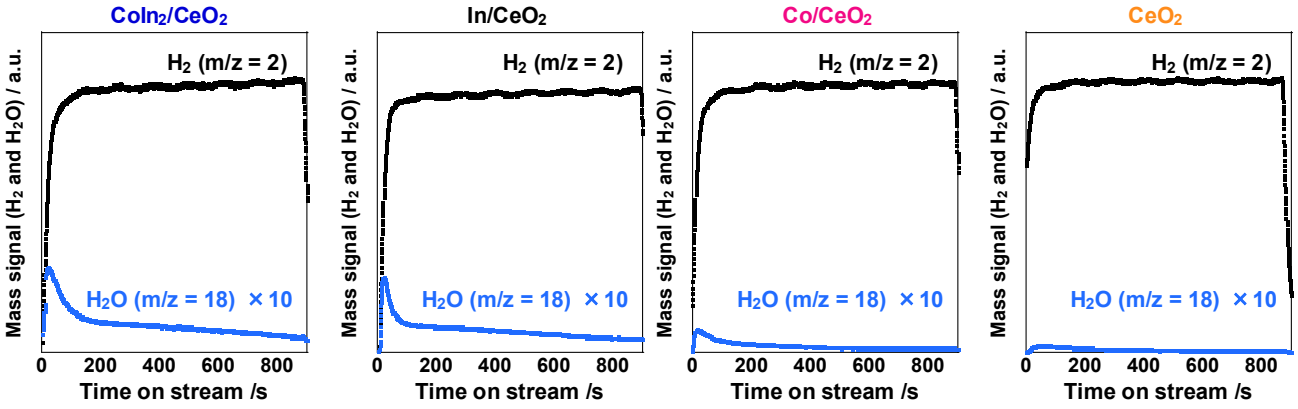

Figure S9. Mass signal of H_2 (m/z = 2) and H_2O (m/z = 18) on the prepared OCs (20wt% $CoIn_2/CeO_2$, 15.9wt% In/CeO_2, 4.1wt% Co/CeO_2 and CeO_2) during the reduction step.

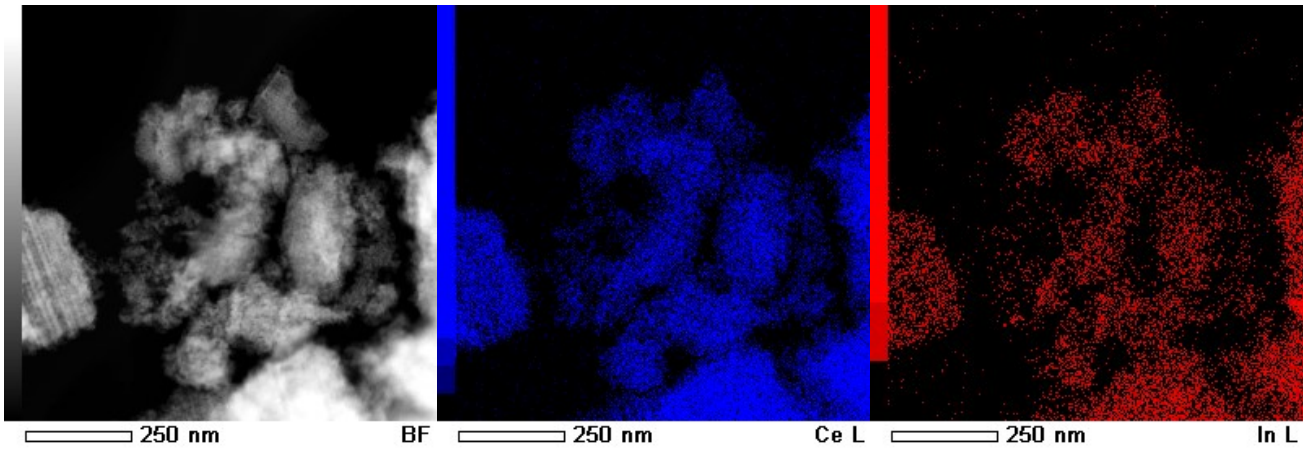

Figure S10. EDX mapping images of 15.9wt% In/CeO_2 after the reduction step.

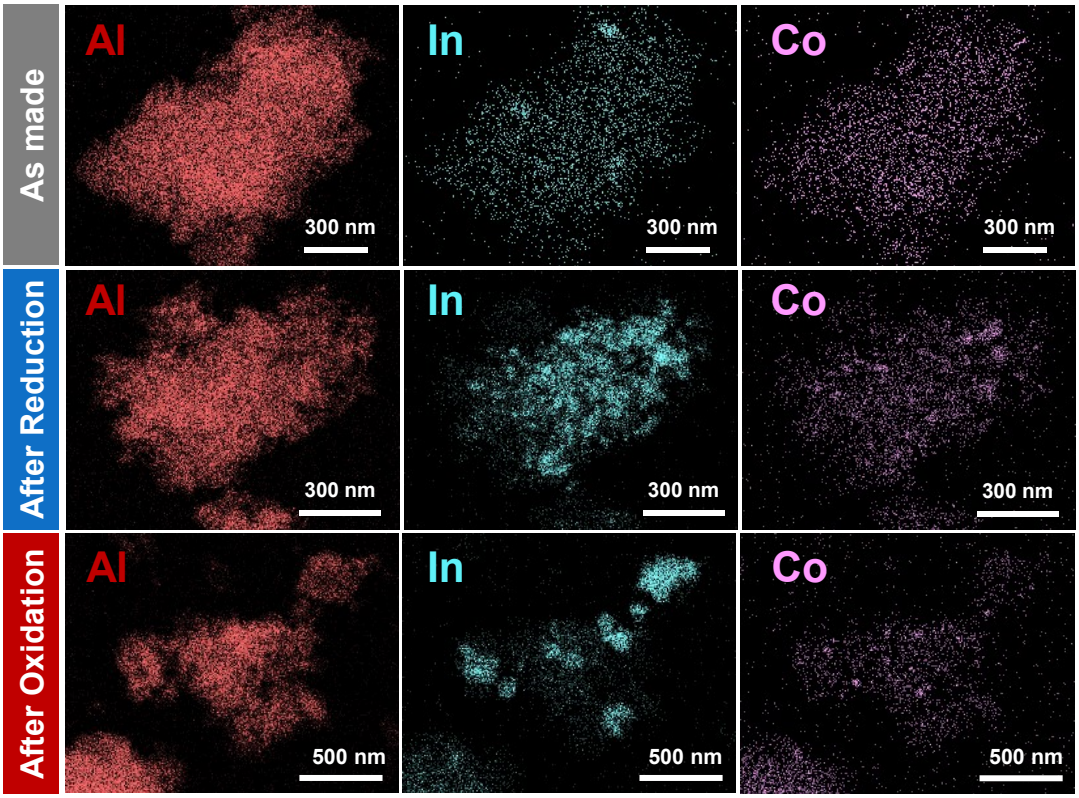

Figure S11. EDX mapping images for $CoIn_2/Al_2O_3$ before and after RWGS-CL cycle test.

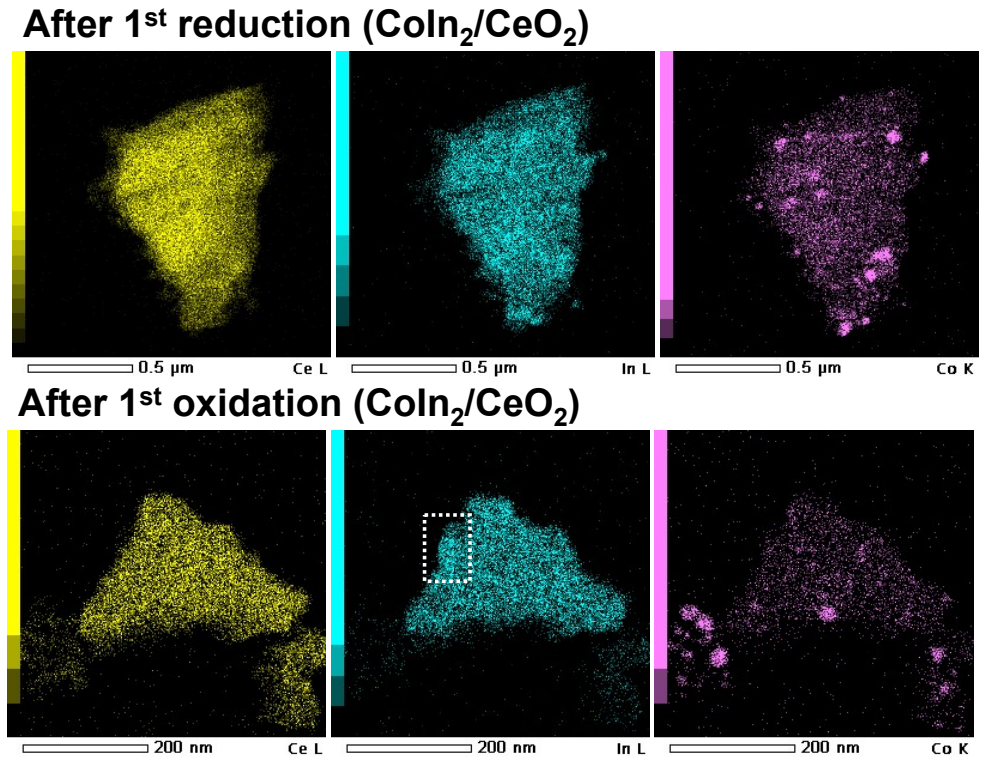

Figure S12. EDX mapping images of $CoIn_2/CeO_2$ (after 1st RWGS-CL cycle).

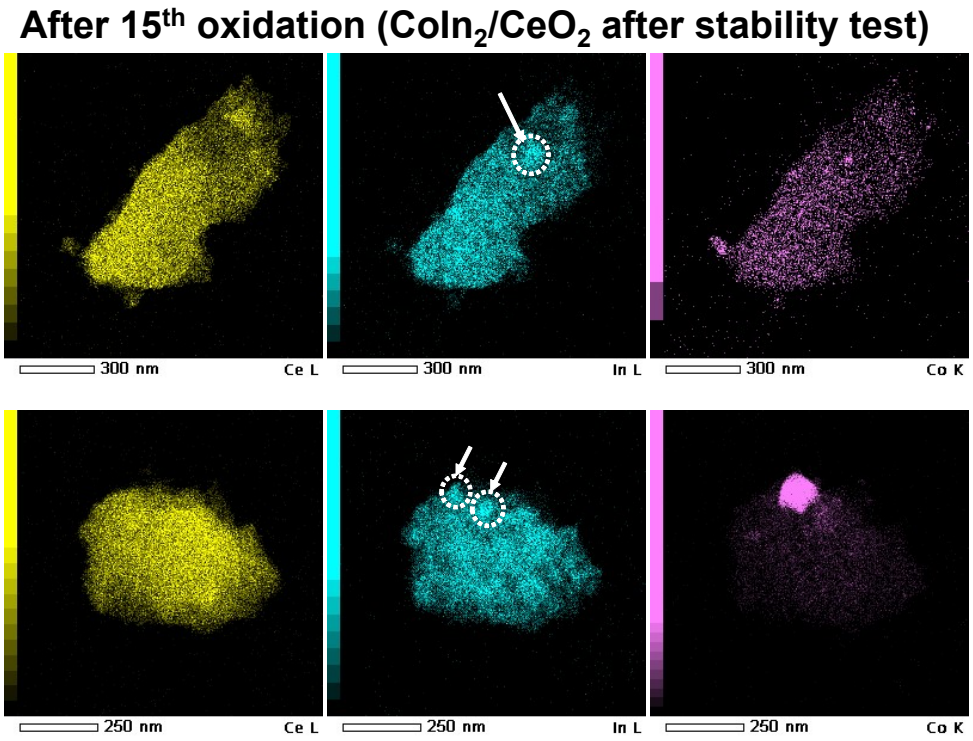

Figure S13. EDX mapping images of CoIn2/CeO2 after 15th oxidation step (stability test).

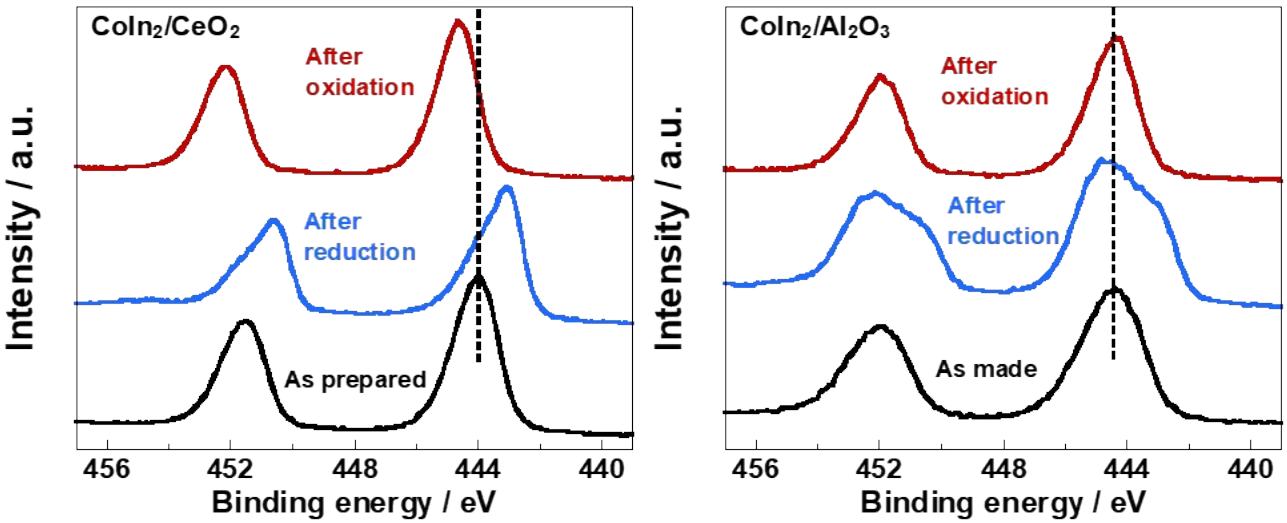

Figure S14. XPS spectra of the In3d region for $CoIn_2/CeO_2$ and $CoIn_2/Al_2O_3$

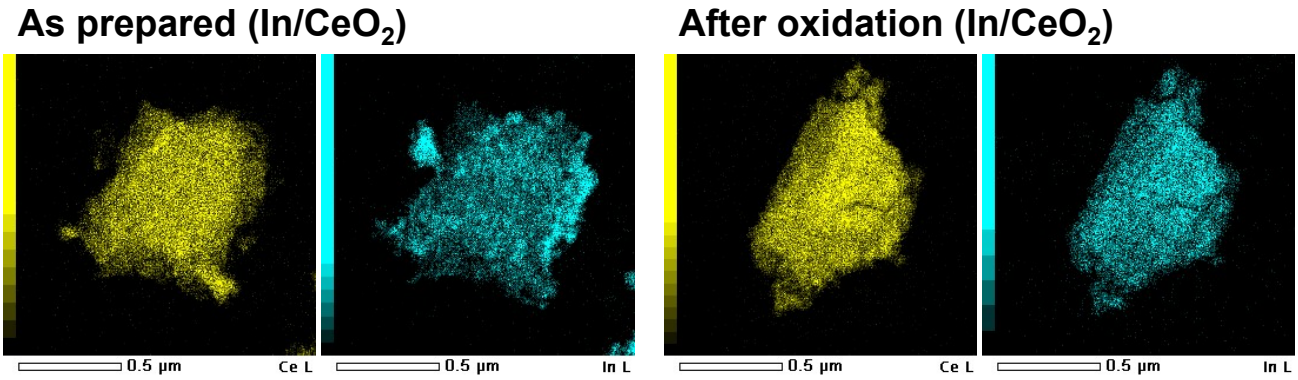

Figure S15. EDX mapping images of In/CeO_2 (As-prepared and after oxidation step).

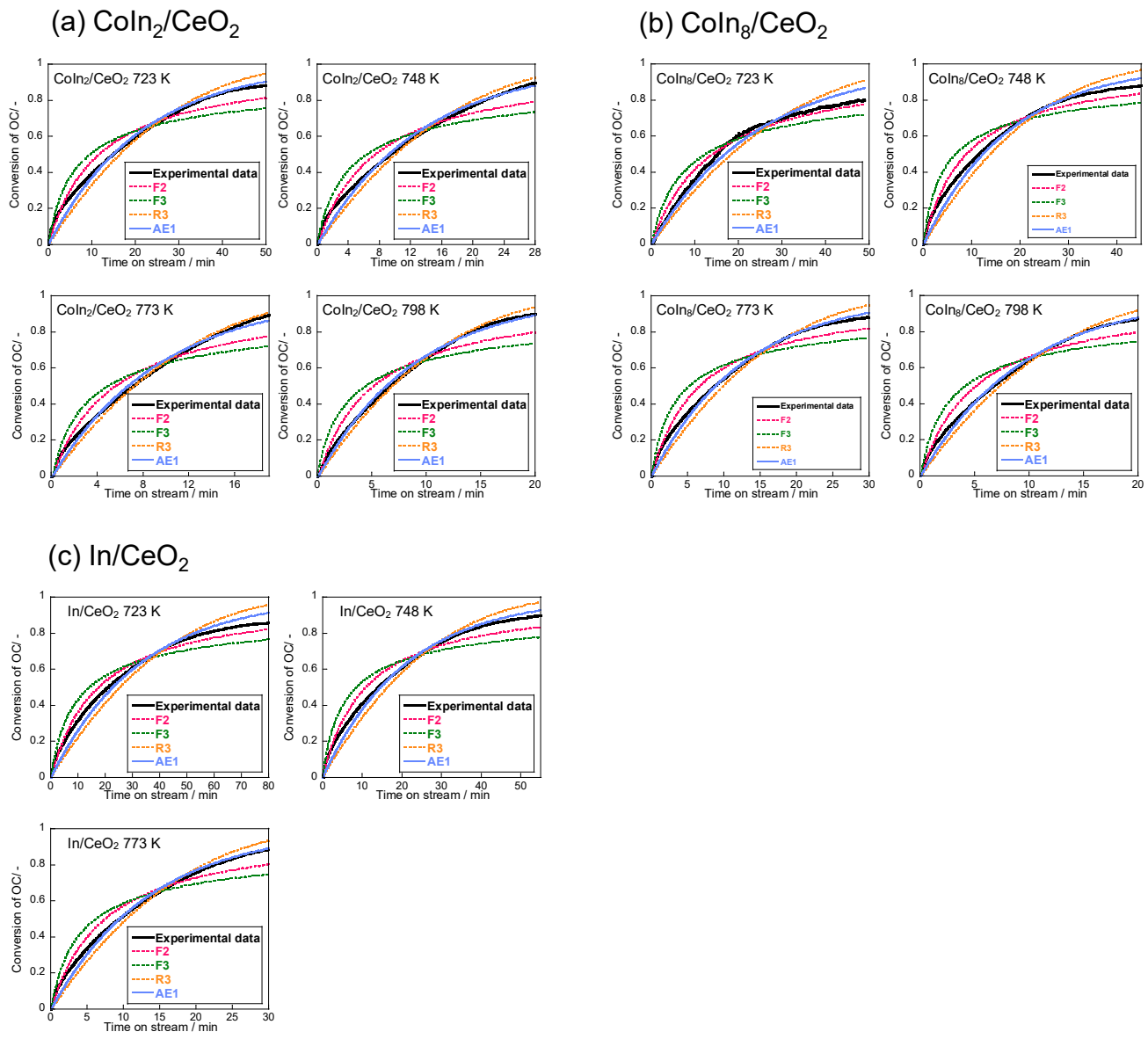

Figure S16 Comparison of experimental data for reduction of (a) $CoIn_2/CeO_2$, (b) $CoIn_8/CeO_2$ and (c) In/CeO_2 by H_2 with Avrami Erofe'ev model (AE1), phase-boundary controlled reaction model (R3), third order model (F3) and second order model (F2).

In this study, experimental data for reduction step were obtained by thermogravimetric analysis (TGA). The reduction conversion was defined by the following equation:

$$x(reduction) = \frac{m_i - m_t}{m_i - m_f}$$

where m_i is the initial mass, m_t is the mass at time t, and m_f is the final mass of the oxide after complete reduction. From the values of solid-state conversion x and reaction time t, plots of $\ln[-\ln(1-x)]$ vs. $\ln(t)$ were constructed, and the slope of each plot was used to identify the most appropriate kinetic model. In the present analysis, the slopes obtained for all oxygen carriers were in the range of approximately 0.8–1.2. Accordingly, four kinetic models were considered as candidates: the

Avrami–Erofe'ev model (AE1), the phase-boundary-controlled reaction model (R3), the third-order reaction model (F3), and the second-order reaction model (F2). By comparing the experimental data with the calculated conversion profiles and evaluating the root mean square deviation (RMSD), the AE1 model was found to provide the best fit to the experimental results.

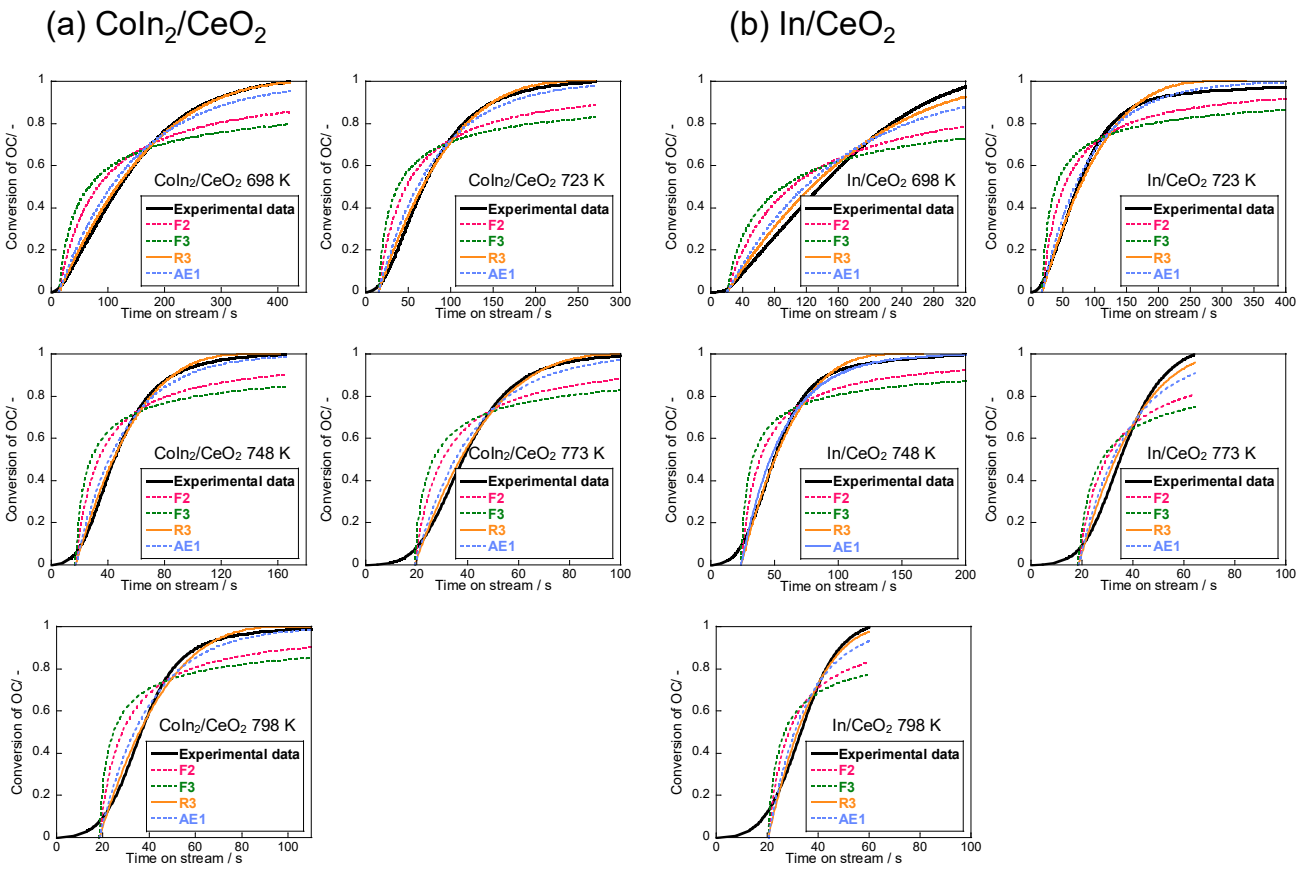

Figure S17 Comparison of experimental data for oxidation of (a) $CoIn_2/CeO_2$, (b) In/CeO_2 by CO_2 with Avrami Erofe'ev model (AE1), phase-boundary controlled reaction model (R3), third order model (F3) and second order model (F2).

Table S1. Performance for CO production on the prepared OCs at the oxidation step.

Oxygen carrier	CO production [b] /mmol	CO yield [b] / mmol g_{oc}^{-1}	CO yield per gram of $CoIn_2$ [b] / mmol g_{CoIn2}^{-1}	Reduction degree / %	Oxidation completion time [b] /s	STY of CO [b] / mmol g_{oc}^{-1} h^{-1}	STY of CO per gram of $CoIn_2$ [b] / mmol g_{CoIn2}^{-1}	Overall CO_2 conversion [b] / %
20wt% $CoIn_2$/ CeO_2	0.313	2.08	10.4	83.8	240	31.2	156	17.5
Co-In_2O_3[a]	0.318	2.11	10.6	23.4	678	11.2	56.0	6.3
20wt% $CoIn_2$/ γ-Al_2O_3	0.187	1.43	7.15	68.8	413	12.5	62.5	6.1
20wt% $CoIn_2$/ r-TiO_2	0.273	1.82	9.10	79.2	599	11.0	55.0	6.1
20wt% $CoIn_2$/ a-TiO_2	0.287	1.91	9.55	83.5	1008	6.8	34.0	3.8
20wt% $CoIn_2$/ SiO_2	0.210	1.40	7.00	67.3	1011	5.1	25.5	2.8

[a] Co/In = 0.5, 16.5wt% Co loaded on In_2O_3, [b] Average values of 3 cycle

Table S2. H_2O yields on the prepared OCs during the reduction step.

Oxygen carriers	H_2O yield / mmol g^{-1}				CO yield[a]
	1st cycle	2nd cycle	3rd cycle	Average of 2nd and 3rd cycle	
$CoIn_2/CeO_2$	3.04	2.18	2.16	2.17	2.08
$Co\text{-}In_2O_3$	6.07	1.93	2.17	2.05	2.11
$CoIn_2/\gamma\text{-}Al_2O_3$	2.55	1.77	1.62	1.69	1.43
$CoIn_2/r\text{-}TiO_2$	2.63	1.94	1.90	1.92	1.82
$CoIn_2/a\text{-}TiO_2$	2.89	1.81	1.94	1.87	1.91
$CoIn_2/SiO_2$	2.68	1.57	1.37	1.47	1.40

[a] CO yield reported in Table S1

Table S3. The summary of the performance on 20wt% $CoIn_2/CeO_2$ during the stability test.

Cycle number	CO yield /mmol g^{-1}	Reduction degree / %	Space-time Yield /mmol g^{-1} h^{-1}	Overall CO_2 conversion / %
1	2.05	82.5	35.0	19.6
2	1.97	79.2	33.6	18.8
3	1.95	78.5	32.2	18.0
4	1.92	77.4	32.0	17.9
5	1.91	76.9	31.6	17.7
6	1.90	76.5	31.1	17.4
7	1.89	76.3	30.7	17.2
8	1.90	76.3	30.2	16.9
9	1.89	76.0	30.7	17.2
10	1.88	75.9	30.2	16.9
11	1.89	76.0	30.1	16.8
12	1.87	75.3	30.5	17.1
13	1.87	75.4	30.4	17.0
14	1.87	75.3	30.4	17.0
15	1.87	75.3	30.7	17.2

Table S4. Summary of the performance on Co-In_2O_3 and 20wt% $CoIn_2/CeO_2$ at the oxidation step using 100vol% CO_2.

Oxygen carrier	GHSV / h^{-1}	CO yield / mmol g^{-1}	Max. CO_2 conversion / %	Total CO_2 conversion / %
Co-In_2O_3	5700	2.31	81.8	3.7
	4080	2.77	81.1	6.0
	2450	2.71	75.2	9.5
20wt% $CoIn_2/CeO_2$	5700	1.87	100	12.4
	4080	1.83	100	15.4
	2450	1.84	100	20.6

Table S5. Comparison of 20wt% $CoIn_2/CeO_2$ to other reported supported-type oxygen carriers for RWGS-CL.

Material	Temperature / K	CO_2 concentration / %	CO yield / mmol g^{-1}	STY of CO / mmol g^{-1} h^{-1}
20wt% $CoIn_2/CeO_2$	723	10	1.20	12.9
	773	10	2.08	31.2
	823	10	2.17	37.6
40wt% Fe_2O_3/ZrO_2	773	5	-	ca. 20.7
25wt% $La_{0.8}Sr_{0.2}FeO_3$/SBA-15	873	12.5	2.80	16.8
25wt% $La_{0.75}Sr_{0.25}FeO_3/SiO_2$	873	10	0.65	12[a]
ZrO_2-modified Fe_2O_3 (Fe_2O_3 content = 10wt%)	923	30 or 100	-	31
60wt% $Fe_2O_3/La_{0.1}Sm_{0.1}Ce_{0.8}O_{2-\delta}$	923	10	8.93	35.7
50wt% $La_{0.75}Sr_{0.25}FeO_3$/SBA-15	973	10	ca. 2	ca. 6.0
50mol% $CeO_2 \cdot Ca_2Fe_2O_5$	973	20	-	32.7
70wt% Fe_2O_3/GDC-30	1023	10	10.8	46.2
10-Mg-Al-Fe-O (Fe_2O_3 content = 10wt%)	1023	5	1.16	17.6
10wt% Fe_2O_3-$MgAl_2O_4$	1023	40	-	176.4

[a] peak rate of CO production

Table S6. BET specific surface area of each supported $CoIn_2$ OCs before and after RWGS-CL cycle.

Oxygen carrier	As made / $m^2\ g^{-1}$	After reduction / $m^2\ g^{-1}$	After oxidation / $m^2\ g^{-1}$
20wt% $CoIn_2/CeO_2$	58.5	20.1	18.8
Co-In_2O_3	10.1	4.4	3.0
20wt% $CoIn_2/\gamma$-Al_2O_3	137.2	102.2	114.9
20wt% $CoIn_2/SiO_2$	96.0	92.3	88.8
20wt% $CoIn_2$/a-TiO_2	64.5	39.9	46.7
20wt% $CoIn_2$/r-TiO_2	41.8	33.0	30.4

Table S7. H_2O yields on OCs prepared with different Co/In ratios during the reduction step

Oxygen carriers	H_2O yield / mmol g^{-1}				CO yield[b] / mmol g^{-1}
	1st cycle	2nd cycle	3rd cycle	Average of 2nd and 3rd cycle	
4.1wt% Co/CeO_2	0.933	0.331	0.304	0.32	0.07
CeO_2	0.00	0.00	0.00	0.00	0.07

[b] CO yield reported in Table 1

Table S8. Ratio of elements for 20wt% $CoIn_2/CeO_2$ after RWGS-CL cycle tests.

Sample	Ratio of elements measured by ICP / %		
	In	Co	Ce
After1st cycle	22.3	4.9	72.8
After stability test	22.2	4.9	72.9

Table S9. The performance for CO production at the oxidation step on the OCs with different Co loading.

Oxygen carrier	Co / wt%	In / wt%	Co/In ratio	CO production /mmol	CO yield / mmol g^{-1}	Reduction degree / %	STY of CO / mmol g^{-1} h^{-1}	Overall CO_2 conversion [a] / %
$CoIn/CeO_2$	8.2	15.9	1	0.307	2.05	90.6	33.9	18.9
$CoIn_2/CeO_2$	4.1	15.9	0.5	0.313	2.08	83.8	31.2	17.5
$CoIn_4/CeO_2$	2.1	15.9	0.25	0.288	1.92	85.5	29.2	16.3
$CoIn_8/CeO_2$	1.0	15.9	0.125	0.294	1.96	90.6	28.7	16.0
In/CeO_2	0	15.9	0	0.219	1.46	73.1	36.0	20.2

[a] Average values of 3 cycle

Table S10. H_2O yields on OCs prepared with different Co/In ratios during the reduction step

Oxygen carriers	Co/In ratio / -	H_2O yield / mmol g^{-1}				CO yield[c] / mmol g^{-1}
		1st cycle	2nd cycle	3rd cycle	Average of 2nd and 3rd cycle	
$CoIn/CeO_2$	1	4.58	2.25	2.13	2.19	2.05
$CoIn_4/CeO_2$	0.25	2.53	2.02	1.95	1.99	1.92
$CoIn_8/CeO_2$	0.125	2.43	2.09	2.00	2.04	1.96
In/CeO_2	0	2.16	1.67	1.53	1.60	1.46

[c] CO yield reported in Table S9